

Synthesis of Dihydrobenzofuro[3,2-*b*]chromenes as Potential 3CLpro Inhibitors of SARS-CoV-2: A Molecular Docking and Molecular Dynamics Study

Sudip Gorai,^[a, b] Vivek Junghare,^[c] Kshama Kundu,^[a] Sowmomita Gharui,^[d] Mukesh Kumar,^[b, e] Birija Sankar Patro,^[a, b] Sandip K. Nayak,^[a] Saugata Hazra,^{*, [c]} and Soumyaditya Mula^{*, [a, b]}

The recent emergence of pandemic of coronavirus (COVID-19) caused by SARS-CoV-2 has raised significant global health concerns. More importantly, there is no specific therapeutics currently available to combat against this deadly infection. The enzyme 3-chymotrypsin-like cysteine protease (3CLpro) is known to be essential for viral life cycle as it controls the coronavirus replication. 3CLpro could be a potential drug target as established before in the case of severe acute respiratory syndrome coronavirus (SARS-CoV) and Middle East respiratory syndrome coronavirus (MERS-CoV). In the current study, we wanted to explore the potential of fused flavonoids as 3CLpro inhibitors. Fused flavonoids (5a,10a-dihydro-11*H*-benzofuro[3,2-*b*]chromene) are unexplored for their potential bioactivities due to their low natural occurrences. Their synthetic congeners are also rare due to unavailability of general synthetic methodology. Here we designed a simple strategy to synthesize 5a,10a-dihydro-11*H*-benzofuro[3,2-*b*]chromene skeleton and its four

novel derivatives. Our structural bioinformatics study clearly shows excellent potential of the synthesized compounds in comparison to experimentally validated inhibitor N3. Moreover, *in-silico* ADMET study displays excellent druggability and extremely low level of toxicity of the synthesized molecules. Further, for better understanding, the molecular dynamic approach was implemented to study the change in dynamicity after the compounds bind to the protein. A detailed investigation through clustering analysis and distance calculation gave us sound comprehensive data about their molecular interaction. In summary, we anticipate that the currently synthesized molecules could not only be a potential set of inhibitors against 3CLpro but also the insights acquired from the current study would be instrumental in further developing novel natural flavonoid based anti-COVID therapeutic spectrums.

Introduction

The recent emergence of coronaviruses has been considered as the biggest pandemic of this century as it posed a severe threat to the existence of the human population. The novel coronavirus (SARS-CoV-2) has led to a worldwide pandemic with more than approx. 346 million cases and approx. 5.5 million deaths

already reported so far (WHO, 23 Jan, 2022).^[1] However, incomplete vaccination and absence of any promising therapeutic drugs for these coronaviruses limit the countless efforts to prevent the spread of the SARS-CoV-2 worldwide. Coronaviruses belong to the family Coronaviridae, which consist of four genera, a) α -coronavirus, b) β -coronavirus, c) γ -coronavirus and d) δ -coronavirus. The current threat, COVID-19 belongs to the beta genus with approximately 96% identity with the bat coronavirus genome.^[2] The SARS-CoV-2 has a ~32 kb RNA Genome that is considered as the largest one among the reported family members. The viral genome contains nucleosides coding for both structural and non-structural proteins that contribute to basic functions of the coronavirus, including replication, assembly and it interacts with the recognized receptor of the host. The major structural proteins of all coronaviruses are spike glycoprotein (S), envelope proteins (E), membrane proteins (M) and nucleocapsid proteins (N).^[3]

In the therapeutic development against the COVID-19, the main protein targets are non-structural proteins, 3C like protease (3CLpro), RNA-dependent RNA polymerase (RDRP) and a structural protein, Spike glycoprotein (Figure S1). The RDRP is a virus protein and it is mainly essential during the infection phase for the virus. This enzyme is responsible for the transcription and replication of the RNA genome. Spike glycoprotein is the S protein, which facilitates the entry of

[a] S. Gorai, Dr. K. Kundu, Dr. B. S. Patro, Dr. S. K. Nayak, Dr. S. Mula
Bio-Organic Division
Bhabha Atomic Research Centre,
Mumbai-400085 (India)
E-mail: smula@barc.gov.in

[b] S. Gorai, Dr. M. Kumar, Dr. B. S. Patro, Dr. S. Mula
Homi Bhabha National Institute
Anushakti Nagar, Mumbai-400094 (India)

[c] V. Junghare, Prof. S. Hazra
Department of Biotechnology,
Centre for Nanotechnology
Indian Institute of Technology Roorkee (IITR)
Roorkee, Uttarakhand (India)
E-mail: saugata.hazra@bt.iitr.ac.in

[d] S. Gharui
Pondicherry University,
Puducherry-605 014 (India)

[e] Dr. M. Kumar
Radiation Biology and Health Science Division
Bhabha Atomic Research Centre,
Mumbai-400085 (India)

Supporting information for this article is available on the WWW under <https://doi.org/10.1002/cmdc.202100782>

coronavirus to the human host cell by interacting with ACE 2 receptors.

However, 3CLpro is encoded by the ORF 1a/b of corona virus,^[4] which is a replicase part at the 5' side of the corona virus (Figure S2). The amino acid sequence of 3CLpro from SARS-CoV-2 has 96% similarity with the same from SARS.^[5] This enzyme mediates proteolytic processing. It cleaves the replicase polyproteins 1a and 1ab at around 11 sites (nsp 5–16).^[6] This produces non-structural proteins (nsps) which are important for the viral replication and other processes. Thus, 3CLpro plays a crucial role in the processing of the polyproteins. The recognition sequence of this protein has been reported to be Leu-Gln↓(Ser, Ala, Gly) (↓ marks the cleavage site)^[7] and human proteases does not have similar cleavage specificity.^[8] This uniqueness helps 3CLpro inhibitors to supposedly having fewer side effects for the infected animal's system. Due to which, it has been used as a potential drug target against corona virus and drug repurposing trials have been performed against this target.^[9]

The inhibition of 3CLpro has been studied and protein-inhibitor complex structures have been deposited in RCSB.^[10] Among them, the peptide-like compound, 'inhibitor N3', has been crystallized showing binding in the pocket of 3CLpro (PDB id: 6LU7).^[10d] Interaction details of this inhibitor had shown that it interacts with charged residues: GLU 166, polar residues: GLN 189, THR 190, HIS 164, HIS 163 and hydrophobic residues: PHE 140, CYS 145, GLY 143. The peptide part, i.e. ALA-VAL-LEU, of inhibitor N3 was found to be interactive with residues GLU 166, GLN 189 and THR 190 (Figure S3).

Natural products are always good targets for drug development for the simple reason of their biological compatibility.^[11] Recent studies showed that natural products are also effective to develop 3CLpro inhibitors of SARS-CoV-2.^[10a] Earlier, FRET based assay showed that naturally occurring flavonoids like herbacetin, pectolinarin, luteolin, etc. have antiviral activity against coronavirus, SARS-CoV.^[12] Molecular docking studies also revealed that the natural product quercetin-3- β -galactoside (Figure 1A) having flavonoid core possesses promising inhibitory potential against 3CLpro of SARS-CoV as well.^[13] All these results inspired us to check potential antiviral activity of new flavonoids against SARS-CoV-2. Few years back, Chen et al.

isolated a new type of flavonoid compound "(\pm)-Paeoveitol" (Figure 1B) from the root extract of *Paeonia veitchii* which is being used from long time in Chinese folk medicine 'Chuan-Chi-Shao', as analgesic, sedative and cardiovascular agent.^[14] Paeoveitol is a fused flavonoid having general structure of 5a,10a-dihydro-11*H*-benzofuro[3,2-*b*]chromene (Figure 1C). This type of fused flavonoids where a benzofuran ring is unprecedentedly fused at "b" bond to oxygen of a benzopyran ring (6-6-5-6 linkage) are relatively rare in nature^[15] as compared to plentifully available fused isoflavonoids (Pterocarpan, 6a,11a-dihydro-6*H*-benzofuro[3,2-*c*]chromene, Figure 1D).^[16] The chemical structure of the Paeoveitol intrigued us to test its efficacy against SARS-CoV-2. Thus, the flavonoid Paeoveitol had been docked with the 3CLpro to study its binding affinity around the active site and it was clearly fitted in the active site of 3CLpro (Figure S4). The binding energy of Paeoveitol with 3CLpro was observed to be -7 kcal/mol as compared to -4.47 kcal/mol of inhibitor N3.^[17]

Interestingly, this compound was found near to the place of the peptide part of inhibitor N3. The Paeoveitol found to be interacting with residues LEU 141, SER 144 and CYS 145 (Figure S4). The CYS 145 interaction was found to be common in between both inhibitor N3 and Paeoveitol. These findings motivated us to design and develop more about these flavonoids using a multidisciplinary study approach. Unfortunately, the natural abundance and bioavailability of the Paeoveitol is very low, which forced us to develop new fused flavonoids with general structure of Paeoveitol which can be synthesized easily in large scale and having similar or even better interactions with 3CLpro than Paeoveitol. Only few reports are available on synthesis of these novel fused flavonoids based on Diels-Alder cycloaddition reactions.^[18] This intrigued us to devise a synthetic protocol for making this skeleton easily accessible. Herein, we report a simple general synthetic strategy to synthesize 5a,10a-dihydro-11*H*-benzofuro[3,2-*b*]chromene skeleton. Four new fused flavonoid derivatives were synthesized by the developed method. *In-silico* ADMET screening of all the fused flavonoids were done to study different physicochemical properties like cell permeability, lipophilicity and water solubility, and different pharmacokinetics properties like gastro intestinal absorption, blood brain barrier (BBB) permeability, etc. Further, their pumping through cell and degradations through enzymes were also studied. Finally, molecular docking was performed to understand the in depth interaction of these compounds with the protein. Implementing the dynamics study molecular mechanism was studied which enlightened the sound variation of structural and conformational dynamics within the complexes. In addition, a brief explanation of compounds compatibility with the protein was analysed. Through clustering analysis, the dynamic movement pattern during the compounds binding with the protein and populated clusters formed were obtained. The distance calculation also gives extensive analysis of intermolecular interaction within the interacting and catalytic residues of the protein with the compounds to evaluate their potential as 3CLpro Inhibitors for COVID-19 therapeutics.

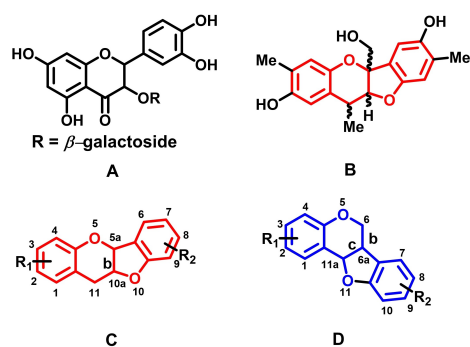


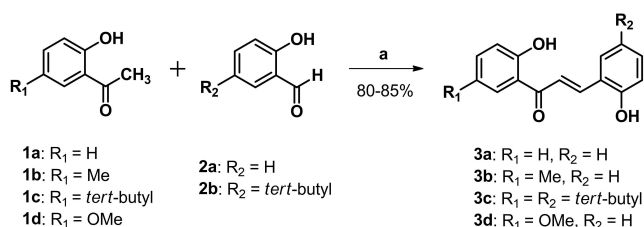
Figure 1. Structure of quercetin-3- β -galactoside (A), (\pm)-Paeoveitol (B) and general structures of 5a,10a-dihydro-11*H*-benzofuro[3,2-*b*]chromene (C) and Pterocarpan (6a,11a-dihydro-6*H*-benzofuro[3,2-*c*]chromene) (D).

Results and Discussion

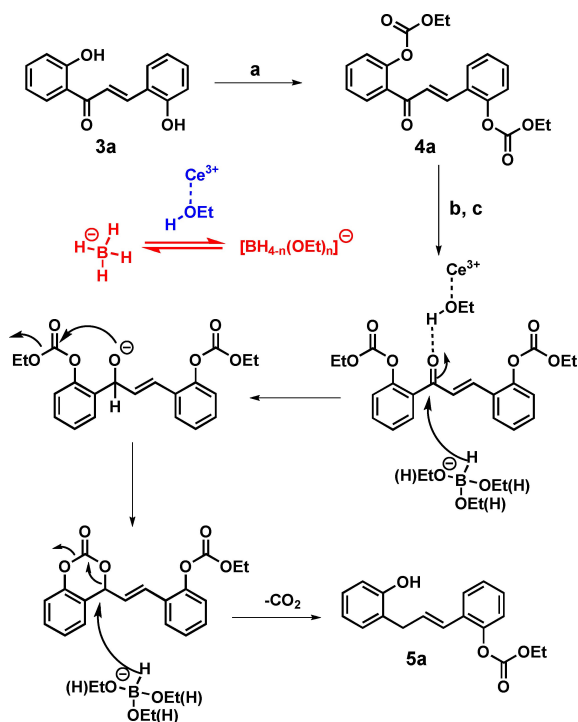
Synthesis

The methodology development started with the synthesis of different substituted dihydroxychalcones (**3a–d**). At first, the base catalyzed Claisen-Schmidt condensation reaction of 2'-hydroxyacetophenones (**1a–d**) was performed with salicylaldehyde derivatives (**2a–b**) that furnished the desired products (**3a–d**) with excellent yields (Scheme 1).

The next challenge was to develop a suitable protocol for chemo-selective reduction of the carbonyl group present in the α,β -unsaturated ketone moiety of **3a** to corresponding 1,3-bis(2-hydroxyphenyl)-propene in good yield. Initial study on Lewis acid promoted 'Luche' type reduction of **3a** with NaBH₄ in presence of AlCl₃^[19] led to the unwanted reduction of the olefinic function of **3a** keeping carbonyl function intact (data not shown).



Scheme 1. Synthesis of substituted dihydroxychalcones **3a–d**. (a) 50% aq. KOH, EtOH, 25 °C, 12 h.

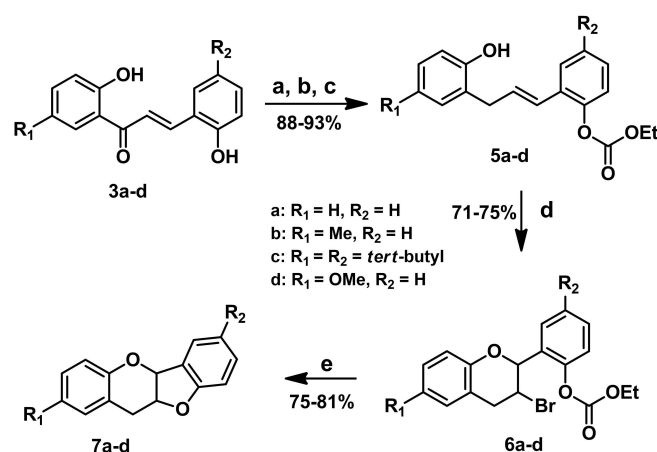


Scheme 2. (a) TEA (2.1 equiv.)/ethyl chloroformate (2.1 equiv.), dry THF, 25 °C, 2 h; (b) CeCl₃·7H₂O (10 mol%), EtOH, 25 °C, 10 min; (c) NaBH₄ (1.2 equiv), EtOH, –5 to 0 °C, 30 min.

Then, chemo-selective reduction of carbonyl group (Luche type 1,2 reduction^[20]) of **3a** using NaBH₄ in presence of CeCl₃·7H₂O/EtOH was tried taking the advantage of *ortho*-hydroxyphenyl group (coming from acetophenone part) attached to the enone functionality.^[21] For this reaction, both the hydroxy groups of chalcone **3a** was protected first as their ethyl carbonate derivative (**4a**) using ethyl chloroformate/triethylamine (Scheme 2). Gratifyingly, reduction of **4a** with CeCl₃ (1.0 equiv.)/NaBH₄(1.2 equiv.)/EtOH furnished the ethyl carbonate derivative of cinnamyl phenol **5a** as a sole product in excellent yield. It is important to note that both reduction of the carbonyl group and selective deprotection of one of the ethyl carbonate groups of **4a** (*ortho* to ketone group) occurred in tandem to afford **5a**. The chemo-selective reduction of **3a** could be explained by hydride transfer to the carbonyl group activated by CeCl₃/ethanol complex.^[21] The resulting alkoxide ion undergoes nucleophilic attack to ethyl carbonate group to form a six-membered cyclic carbonate intermediate. Finally, another hydride attack on the cyclic carbonate with concomitant extrusion of carbon dioxide led to the formation of 2-cinnamyl phenol derivative **5a** (Scheme 2).

Further optimization of the reaction revealed that 10 mol% of CeCl₃·7H₂O is sufficient to afford **5a** in high yield. The catalytic action of CeCl₃ can be explained by the activation of carbonyl group through its co-ordination and subsequent release from co-ordination after hydride transfer process. Moreover, the temperature played a crucial role in controlling the reduction pathway. It was observed that while the reaction at –5 to 0 °C afforded **5a** as a sole product in good yield, reaction at a marginally higher temperature (2–5 °C), 2-(2*H*-chromen-2-yl)phenyl ethyl carbonate (**5'a**, see SI) was formed as a side product along with **5a**. Using the optimized reaction conditions, few more dihydroxychalcones (**3b–d**) were prepared and reduced to corresponding 2-cinnamyl phenols (**5b–d**) in excellent yields (Scheme 3).

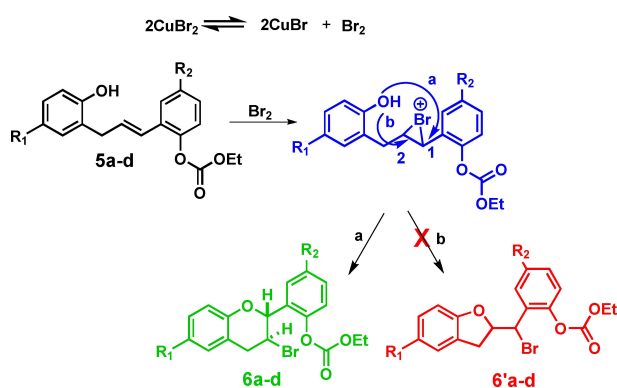
Next, **5a–d** were converted to corresponding 3-bromoflavans (**6a–d**) using an intra-molecular bromo-aryloxylation



Scheme 3. (a) TEA (2.1 equiv.)/ethyl chloroformate (2.1 equiv.), dry THF, 25 °C, 2 h; (b) CeCl₃·7H₂O (10 mol%), EtOH, 25 °C, 10 min; (c) NaBH₄ (1.2 equiv.), EtOH, –5 to 0 °C, 30 min; (d) CuBr₂ (2.1 equiv.), dry ACN, 25 °C, 5–12 h; (e) 25% aq. NH₄OH, MeOH, 25 °C, 12 h.

strategy. Cu(II) bromide is known to be a mild brominating agent that dissociates to release Br₂ along with Cu(I) bromide in equilibrium.^[22] Earlier, CuBr₂ mediated intra-molecular cyclization reaction was reported in synthesizing benzo[*b*]furan/benzo[*b*]pyran derivatives from substituted phenols.^[23] All of these inspired us to use similar reaction condition in the present scenario. Gratifyingly, the reaction of **5a–d** with Cu(II) bromide in ACN clicked well as per our expectation and furnished desired products **6a–d** in good yields. The formation of the products can be explained by a mechanism where first three membered bromonium ion was formed at the olefinic site followed by *in situ* intramolecular cyclo-etherification reaction occurred at benzylic carbon (carbon at 1, Scheme 4) by a regioselective S_N2 type attack of the free hydroxyl group present in proximity. The predominant formation of products **6a–d** is controlled by the greater electrophilicity of the benzylic carbon (path a; Scheme 4) and other possible products **6'a–d** did not form at all (path b; Scheme 4). In all the cases only single trans-diastereomer is obtained which was quite obvious due to the stereo-specific nature of the reaction. The trans geometry of the products **6a–d** are confirmed by the observed coupling constant (*J*) values of 8–9 Hz in ¹H NMR spectra which are comparable with the reported *J* values of closely related 3-iodochromans.^[24]

With the 3-bromoflavan derivatives **6a–d** in hand, final step to construct the targeted compounds i.e., substituted 5a,10a-dihydro-11*H*-benzofuro[3,2-*b*]chromenes, **7a–d** were attempted. It was envisioned that deprotection of the carbonate functionality will regenerate the hydroxyl group and then an intra-molecular cyclo-etherification will lead to the formation of the target compounds. Initially, different mild reaction conditions like NaBH₄ mediated hydrolysis and catalytic hydrogenolysis reaction were tried, but all these efforts were unsuccessful. On the other hand, under strong reaction condition, the reaction showed erratic behaviour. For example, lithium aluminium hydride (LAH) mediated hydrolysis of **6c** furnished the target product **7c** (25% yield) directly instead of otherwise expected corresponding hydroxy product (carbonate deprotected product of **6c**). But, the reaction did not work well with the other substrates like **6a–b** and **6d**. For **6a** and **6b**,



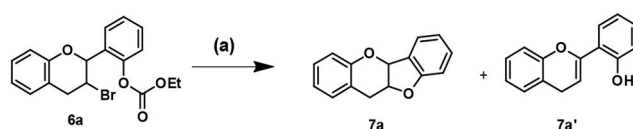
Scheme 4. Proposed mechanism of the synthesis of **6a–d** by bromination/intramolecular cyclo-etherification tandem reaction.

probably the chroman rings were broken to non-characterizable side products. Whereas for **6d**, the reaction furnished **7d** with very low yield (10%).

All these observations hinted that hydrolysis of carbonate group and cyclo-etherification can be done in tandem probably under some milder reaction condition. Then, we thought of using mild basic condition as there is a fair chance that strong basic condition can trigger an unwanted dehydrobromination reaction. After the extensive literature survey on recent advancement in carbonate hydrolysis in mild basic condition, we found that recently L. Panzella *et al.* easily deprotected carbonate group to hydroxyl group by treating with aq. NH₄OH solution in synthesizing hydroxycinnamyl alcohol derivative using a decade old protocol.^[25] This reaction condition was tried in our system. As per the expectation, under aq. NH₄OH reaction condition at 25 °C, **6a** successfully followed the tandem route i.e. deprotection of carbonate group and thereafter cyclization to yield **7a** without yielding any uncyclized decarbonated product (Scheme 3).

Optimization of the reaction condition established that with increase in reaction time at 25 °C, the yield of **7a** gradually increased giving the maximum yield (75%) after 12 h. Under refluxing conditions, the deprotection of carbonate group occurred but it was associated with concomitant dehydrobromination to yield **7a'** and a trace amount of **7a** was also isolated there (Scheme 5). The rationale behind this observation may be, at elevated temperature it can cross the activation barrier to initiate dehydrobromination reaction even in the weak alkaline condition whereas at room temperature the reaction becomes kinetically controlled. Finally, using this optimized protocol, all the 3-bromoflavan derivatives **6a–d** were successfully transformed into 5a,10a-dihydro-11*H*-benzofuro[3,2-*b*]chromenes **7a–d** in excellent yields (Scheme 3). It is important to mention that all the reactions furnished single diastereomer which supports a diastereospecific S_N2 type pathway for the final cyclization reaction.

The structures of the 5a,10a-dihydro-11*H*-benzofuro[3,2-*b*]chromenes, **7a–d** were characterized by NMR spectroscopy.



Entry	Condition (a)	yield of 7a ^[a]	yield of 7a' ^[a]
1	25% aq. NH ₄ OH, 25 °C, 2 h	22	-
2	25% aq. NH ₄ OH, 25 °C, 5 h	35	-
3	25% aq. NH ₄ OH, 25 °C, 12 h	75	-
4	25% aq. NH ₄ OH, reflux, 2 h	trace	25
5	25% aq. NH ₄ OH, reflux, 12 h	trace	85

Scheme 5. Optimization of cyclo-etherification reaction of **6a**. [a] Isolated % yield.

For example, in **7c**, typical doublet at 5.63 ppm and a multiplet at 5.24–5.20 ppm in ^1H NMR, and peaks at 82.4 and 79.3 ppm in ^{13}C NMR support the formation of fused skeleton. Most importantly, the observed coupling constant (J) value of 7.0 Hz for the doublet at 5.63 ppm confirmed *cis* geometry of the skeleton.^[18a] See also the ORTEP renderings of **7c** and **7d** in Figure 2.

Molecular electrostatic potential (MEP)

The potential inhibitor development for an enzyme needs to examine the interaction profile between the enzyme and target small molecules. The active site or recognition sites of enzymes are usually on the surface or in a void pocket. Hence, the surface of a small molecule is essential for binding. In this direction, the Molecular Electrostatic Potential (MEP) had been evaluated for all the fused flavonoids (**7a–d**). The MEP surfaces have mainly three components i.e. electropositive (blue), electronegative (red), and null value region (green/white). It highlights the hydrogen bond acceptor and donor regions of compounds (Figure 3). The MEP surface mappings are very useful to explain the potential binding affinity of the compounds towards the 3CLpro enzyme as discussed *vide infra*.

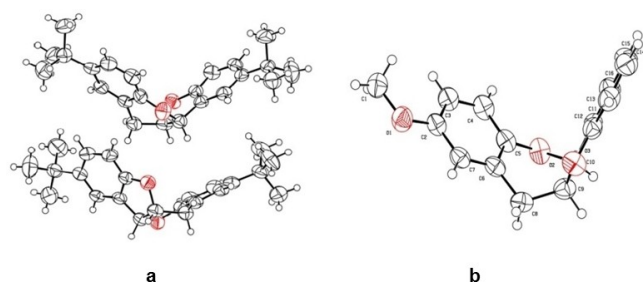


Figure 2. Orthogonal ORTEP views of the crystal structure of compounds **7c** (a) and **7d** (b).

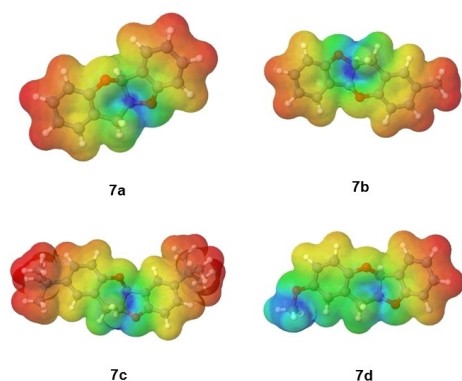


Figure 3. Molecular Electrostatic Potential (MEP) of **7a–d**.

Molecular docking study

Binding affinity with 3CLpro

The docking with 3CLpro enzyme of SARS-CoV-2 of all the final compounds (**7a–d**) was performed according to the template used for docking (PDB id 6lu7) with inhibitor N3.^[10d] First, **7a** was docked with the 3CLpro. It resulted in AutoDock score -6.9 kcal/mol (Table 1). This compound was found to be in the active site and CYS 145, HIS 41, MET 49 and GLN 189 were within the 4 \AA distance (Figure S5, and Table S3). Similarly, docking of other compounds **7b–7d** was done (Figure 4, S6, S7 and Table S3) and their AutoDock scores were observed as -7.6 , -7.3 and -7.1 kcal/mol respectively (Table 1). The parameters used for executing the docking analysis, the center Grid box was in x, y, z dimensions were taken as 64.039, 46.852, 58,802 respectively. The spacing was taken as 1 Angstrom.

Ligand	7a	7b	7c	7d
AutoDock Score [kcal/mol]	-6.9	-7.6	-7.3	-7.1

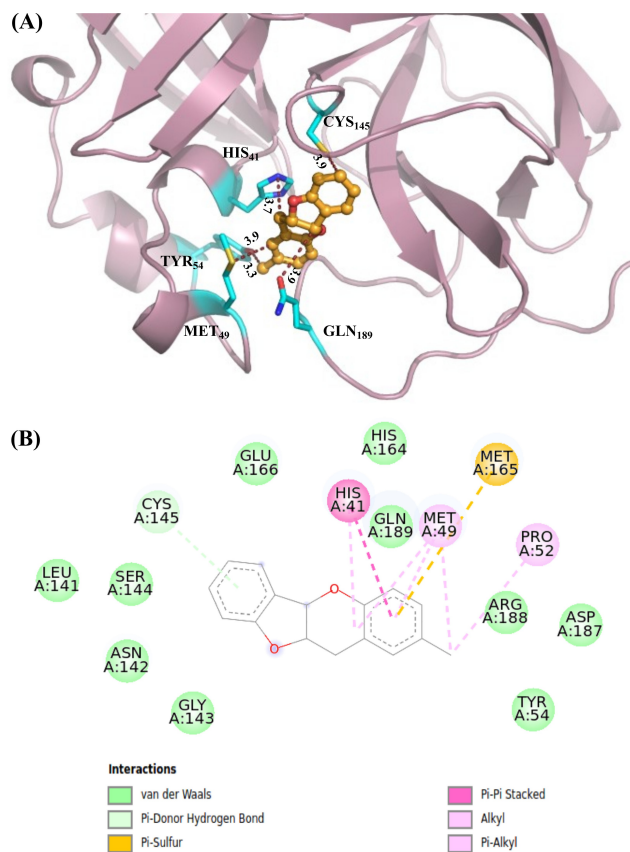


Figure 4. The interaction between 3CLpro and the compound **7b**. A) The enzyme is in cartoon representation and compound in ball-stick representation. The interacting residues were shown in the stick from with their distances in dashes. B) The two-dimensional representation of interacting residues.

While the number of points in x, y, z dimensions were taken as 19, 22, 20 respectively and the number of modes were selected as 10 for the docking analysis. Thus, all the fused flavonoids have shown high AutoDock score towards 3CLpro enzyme.

The interaction between all the fused flavonoids, **7a–d** and the 3CLpro enzyme had been analyzed to gather their binding profile. Most of the residues in the catalytic domain of inhibitor N3 were also shown interaction with the compounds. The residues HIS 41, MET 49, TYR 54, PHE 140, ASN 142, SER 144, CYS 145, HIS 163, HIS 164, MET 165, GLU 166, ASP 187, ARG 188, GLN 189, GLN 192 were found to be interacting with compounds. The binding pocket is surrounded by the beta-sheets structure with a small helix (Figure S8).

Further, the compound interactions were evaluated out by finding residues within 4 Å and have been enlisted in Table S3. These compounds had shown less polar contacts. Only for compound **7d** few polar contacts have been observed. The highest binding energy compound, **7b** has been shown with its interacting residues (Figure 4). Rest interactions can be found in Figures S5–S7.

Orientation of compounds in the active site of 3CLpro

All compounds had been observed to be placed in the catalytic domain of 3CLpro, as shown in Figure 5B. The docking template used, i.e. PDB id 6LU7,^[10d] had an inhibitor N3 bound in the active site (Figure 5A). This is a peptide-like inhibitor and the binding energy had been reported to -4.47 kcal/mol.^[17] All the fused flavonoids used in the present study had binding affinity greater than -6.9 kcal/mol.

Further, the catalytic site of 6LU7 was found to be a deep cavity-like structure (Figure 5B). The binding of all compounds clearly showed that they were well fitted in the catalytic pocket (Figure 5B, C). This domain has both electropositive and electro-

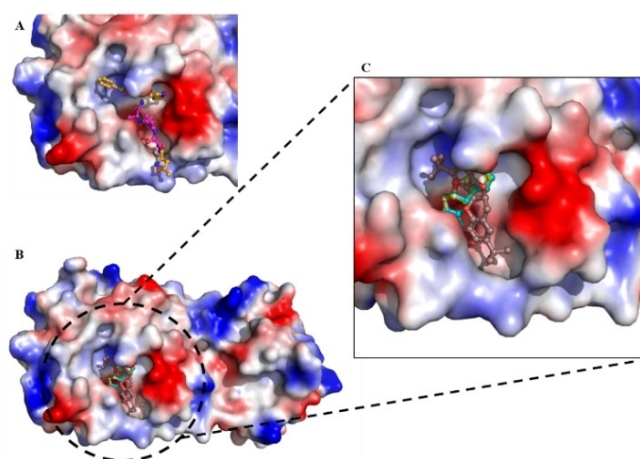


Figure 5. The surface representation of enzyme and binding pocket. A) The inhibitor N3 bound structure of PDB id 6LU7. The inhibitor N3 is in ball-stick form and a peptide part of it, is represented in magenta colour. B) The docking of compounds with 3CLpro enzyme. It shows the binding pocket in a dotted circle with the enzyme in surface representation. C) The catalytic domain where all compounds had been found to be interacting.

negative residues in its vicinity (Figure 5C). Also, the MEP of compounds (Figure 3) had shown the mixture of both electro-negative and electropositive areas. It clearly implies that the compounds have a potential binding affinity towards the 3CLpro enzyme.

Further, the peptide part of inhibitor N3 (Figure 5A) was found to be completely inside the catalytic cavity. Thus, interaction details of this inhibitor had been studied (Figure S9). The peptide part was found to be interactive with residues GLU 166, GLN 189 and THR 190. The interaction analysis of all the compounds, **7a–d** showed that they interact with at least one of these residues. Also, the residue CYS 145, which is at 2.9 Å in case of inhibitor N3 (Figure S9), was found to be within 4 Å of each compound selected in the present study. In addition, the compounds showed interaction with at least one histidine residue found in the vicinity of the active site. Thus, the binding affinity and the interaction profile give support to the potential binding in the active site of 3CLpro and hence the ability to become a potential inhibitor.

Molecular dynamics (MD) simulations

The backbone variation of protein and complex structures

The Root Mean Square Deviation (RMSD) plot for the backbone of apo protein and complex structures was calculated (Figure 6). It was observed that, after 20 ns, every complex along with the apo structure have all attained a stable state. In the apo structure, the RMSD plot also showed stability after 20 ns but it was later seen that, after 70 ns, it became highly dynamic in nature and showed fluctuations. In case of complex **7a**, the trajectory shown is initially stable while after 85 ns there is a leap of 0.1 nm. While in case of complex **7b**, the trajectory attained the stability after 20 ns and remained the same, after 85 ns there was also a leap observed not more than 0.1 nm but soon became stable. In complex **7c**, the trajectory shows

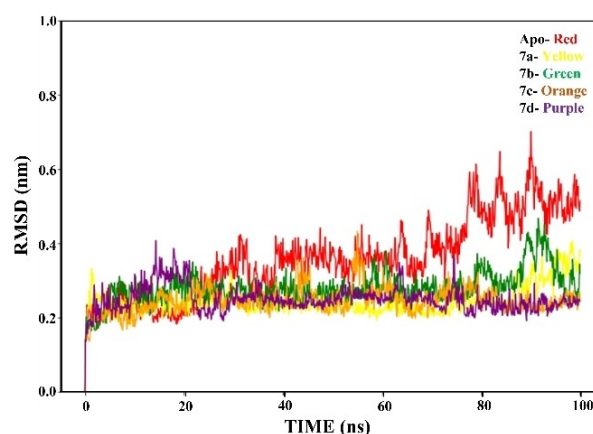


Figure 6. Root Mean Square Deviation (RMSD) of apo and complex structures. The apo, complex **7a**, complex **7b**, complex **7c**, complex **7d** structure plots are represented by red, yellow, green, orange and purple colour graphical representations respectively.

stability with the same fluctuation having a small leap around 55 ns. While in complex **7d**, initially the trajectory was shown with a fluctuation but after 20 ns it became stable. The RMSD fluctuations provides idea about the change in backbone of a protein.^[26] Here, the RMSD plot shows the comparative dynamic behavior of the apo structure as well as the complex formed. It is seen through the plots that **7c** and **7d** have much stable plots while all the ligand complexes (**7a**, **7b**, **7c**, **7d**) have less variation than that of apo structure and hence are more stable than the apo structure. Also, this indicates that complexes formed through the compounds **7a–7d** with 3CLpro reduced the flexibility of protein and gives dynamical conformational stability.^[27]

The residue-wise fluctuations over MD trajectory

Root Mean Square Fluctuation (RMSF) allows us to analyze the fluctuation of residual variation.^[28] It is seen that the variations for all the structures are quite similar, which were highlighted in the pictures with black dotted lines (Figure 7). It is seen that apo, complex **7b**, complex **7c**, complex **7d** have high variation in the F1 region which is the region having Ser 46 to Tyr 54 which also comprises active sites. But a variation in complex **7a** near Thr 225 residue and in complex **7b** near the Ile 152 residue shown high fluctuation. The F2 region of fluctuation, i.e. region near the residues Gln 273 to Met 276 of the protein structure have shown the high fluctuation in the Apo and all the complexes. The fluctuation in all the complexes were much less than the Apo structure which again depicts that the complexes are much stable and lower energy than the Apo, which might be due to the binding with the ligand. The RMSF indicates that residual fluctuations are minimum in complex and the interacting residues in active site has effect of ligand binding.

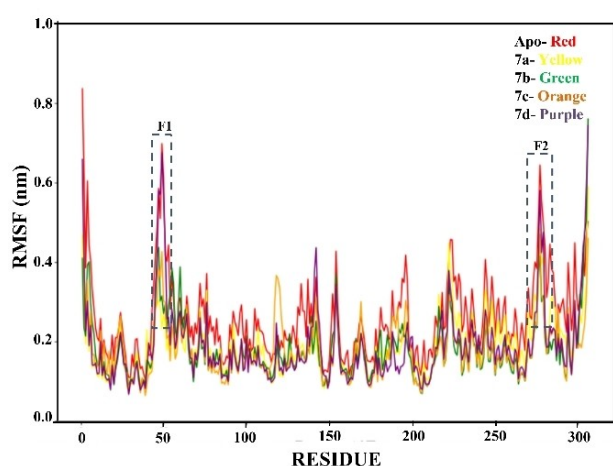


Figure 7. Root Mean Square Fluctuation (RMSF) of apo and complex structures. The apo, complex **7a**, complex **7b**, complex **7c**, complex **7d** are represented by red, yellow, green, orange and purple colour graphical representation respectively.

Radius of gyration analysis

The radius of gyration (Rg) value gives us an idea of how the structural variation affects the compactness of the protein after they are binding with the ligands. The proteins with folded and unfolded confirmation have low and high Rg values respectively. It was seen that the compactness of all the compounds were mostly stable along with the apo (Figure 8). More Rg value indicated high flexibility in protein. Apo protein and complex Rg has shown no significant variation. This shows not much change in the packing of protein. It is seen that the average values of Rg were 2.25 nm, 2.24 nm, 2.23 nm and 2.24 nm for structures complex **7a**, complex **7b**, complex **7c**, complex **7d** respectively while the Apo is 2.21 nm. There is not much huge fluctuation in the average values of Rg and it indicates that not much decrease in globularity of the complexes with respect to Apo protein. The small difference in Rg was expected in complex structures.

Hydrogen bond analysis

Hydrogen bond formation is important to understand the structural integrity of the protein, catalytic region and protein-ligand interaction and it enables us to understand the protein stability and conformation. There is not much considerable change in the hydrogen bond interaction within the protein of all the complexes. The average values of Hydrogen bonds calculated for Apo, complex **7a**, complex **7b**, complex **7c** and complex **7d** are 214, 216, 218, 212, 217 respectively (Figure 9).

Further, that the number of hydrogen bonds were calculated on pairs within 0.35 nm in between protein and ligand complex structures. In complex **7a**, the maximum hits were found of 3 pairs, while for complex **7b**, **7c**, **7d** were 2 but with increasing in value with time variation (Figure S10). This indicated that ligand were able to form hydrogen bond with high frequency of occurring a hydrogen bond. However, the other non-covalent interactions should have contributed to

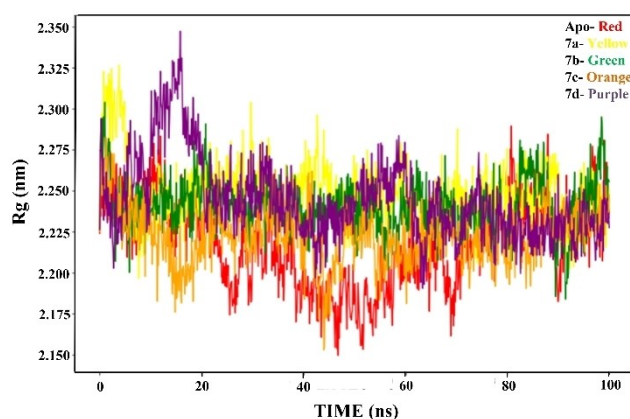


Figure 8. The Radius of Gyration Plot having comparative analysis of the Apo and the complexes; The apo, complex **7a**, complex **7b**, complex **7c**, complex **7d** are represented by red, yellow, green, orange and purple colour graphical representation respectively.

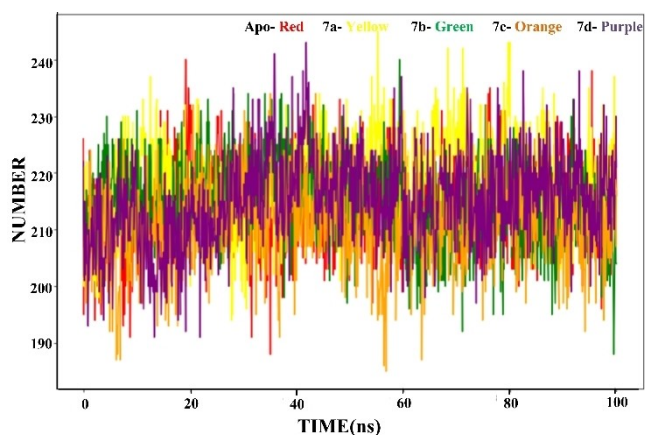


Figure 9. Hydrogen bond Plots having comparative analysis of the Apo and the complexes; The apo, complex 7a, complex 7b, complex 7c, complex 7d are represented by red, yellow, green, orange and purple colour graphical representations respectively.

molecular binding. Thus, to understand their contribution MM/PBSA calculations were performed and discussed *vide infra*.

SASA calculations

The interaction area between the solvent and protein/protein-ligand complexes were calculated and were plotted for each snapshot against the function of time for all the complexes along with the Apo structure. The values for apo, complex 7a, complex 7b, complex 7c, complex 7d are 150.7 nm², 150.1 nm², 152.2 nm², 150.4 nm², 153.73 nm². Higher value of SASA implies more hydrophilicity. The SASA value for complex 7a and complex 7c are low while for complex 7b and complex 7d are high which shows that complex 7a and complex 7c are more accessible to the solvent than that of complex 7b and complex 7d (Figure S11). The SASA has not shown drastic change in complex structures compare to apo protein, but has small change and that was expected for complex structures.

Clustering of simulation trajectory

In cluster analysis, the most populated cluster is considered for analysis as a representative conformation. Clustering analysis was performed on the equilibrated region of the trajectory using the GROMOS algorithm from simulation to get the cluster and their center structures.

The RMSD values for complex 7a, complex 7b, complex 7c, complex 7d are 0.23 nm, 0.225 nm, 0.224 nm and 0.249 nm respectively. It depicts that they must have some conformational change after binding the ligands. It was seen the most cluster formations were formed for all the complexes in structure one. The number of clusters was formed are 4, 6, 7 and 7 for 7a, 7b, 7c and 7d respectively (Figure 10).

Clustering means grouping of very similar structures in one group having less RMSD. The center pdbs from each cluster of a

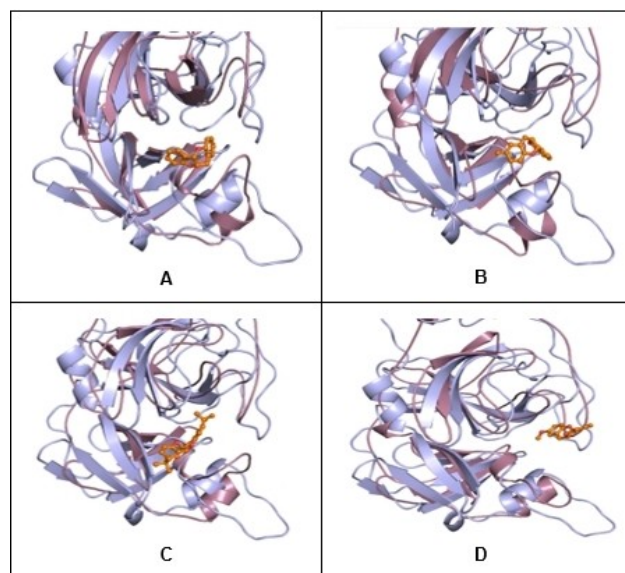


Figure 10. A, B, C, D are the cluster representation of complex 7a, 7b, 7c and 7d respectively. The ligands are represented in a golden ball and stick model. The purple colour representation in all the structures are of the individual complexes whereas the light blue colour cartoon representation are of the Apo structures, where the variation in each loop are observed.

complex system was taken and the pattern was observed (see the Supporting Information animation file). It was observed that the patterns give a probabilistic information about how drug is interacting with the 3CLpro protein and its conformational changes over the simulation. It was observed that the maximum clustering members were found for all the structures in the final portion of trajectory (cluster 1) with most deviating rmsd value from the initial trajectory along with clustering member varying from maximum to least. This enable us to think that the final cluster might be the stable conferred structure for the complex. Moreover, the pattern to represent the above explanation that the drug interaction makes conformational change near the active site and finally, the drug resides in the core. The conformation where drug looks like well fitted in the cavity is a cluster with high number of conformations in it. The detailed interactions have been mentioned in Figure S12–S15 and Table S4.

Further, we have taken this structure from most populated cluster and compared the apo structure (Figure 11). The structural change in the complex structure was observed and hence the RMSD difference was observed. The amino acid residues where variations were seen for each complexes are as follows – for complex 7a: (Ser 1-Met 6), (Ser 46-Asn 51), Thr 224, Thr 226, Asn 274, Gly 275, (Asn 277-Ser 284); for complex 7b: (Ser 46-Leu 50), Phe 223, Thr 224, Gly 278, Arg 279, Gly 283, Ser 284; for complex 7c: (Ser 1-Lys 5), (Ser 46-Asn 51), Thr 224, (Gly 278-Thr 280), (Leu 282-Ala 285), Gln 306 and for complex 7d: (Ser 1-Met 6), (Ser 46-Leu 50), (Phe 223-Thr 226), (Gln 273-Gly 275), (Asn 278-Leu 285). It is seen that in all complexes the fluctuation in the residual region of (Ser 46-Leu 50) and some

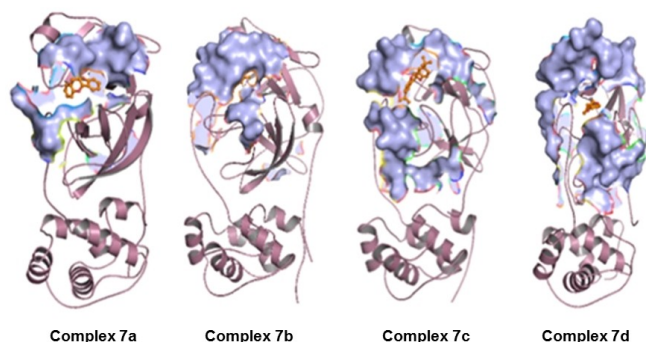


Figure 11. Different most populated clusters of different complexes of **7a** to **7d**.

changes near Gly 278-Ser 284 is constant which might enable us to further investigate in these loops.

Distance variation among compounds and interacting residues

The molecular docking has shown that Gln 189, His 41, Cys 145 were the residues interacting with the ligands. Thus, for the distance calculation, the interaction with the Gln 189 (most interacting residue), His 41, Cys 145 (the dyad of the protease) were chosen to investigate the distance variation with time. The distance was calculated from center of mass and the atom of the residue. In case of Gln 189, the distance variations (highest to lowest) were found in between 0.99–0.34 nm for complex **7a**, 1.16–0.32 nm for complex **7b**, 1.26–0.30 nm for complex **7c**, 0.90–0.34 nm for complex **7d** (Figure S16). For His 41, the variations (highest to lowest) were 0.70–0.40 nm for complex **7a**, 1.1–0.36 nm for complex **7b**, 1.44–0.36 nm for complex **7c** and 1.22–0.38 nm for complex **7d** (Figure S17). Lastly, the distance fluctuation (highest to lowest) observed for Cys 145 were 1.12–0.37 nm for complex **7a**, 1.34–0.50 nm for complex **7b**, 1.25–0.30 nm for complex **7c** and 2.24–0.46 nm for complex **7d** (Figure S18). These variations were from COM of ligands and were expected to show such variation. It indicated that the compounds remained around these catalytic residues and did not jumped from the cavity location and ultimately these suggest that compounds were well fitted in the cavity space.

MM/PBSA calculations

The free binding energy calculation was performed for each system using *g_mmpbsa* tool (Table 2). It was resulted into binding free energy of -114.33 , -128.775 , -136.940 and -96.175 kJ/mol for complex structures with compound **7a**, **7b**, **7c** and **7d** respectively. The van der Waals, electrostatic interactions represent the non-bonded energy component and it was observed to be very low as expected as their contribution was expected to higher for good binding. Further, polar solvation and SASA (non-polar) energy components were calculated and they had contributed less as compared to non-bonded. Thus, the free binding energy of all ligand was found less negative indicating good binding. The compound **7c** has higher binding energy and **7d** is less among all.

ADMET screening

The compound designed for having potential drug value should have properties to have a therapeutic dose value. Thus, to filter its bioavailability criteria the ADMET values are important. In the physicochemical properties of all the compounds, **7a–d**, the molecular weight of all compounds has been found less than 500 g/mol. Additionally, the rotatable bond, hydrogen bond acceptors, hydrogen bond donor and topological polar surface area (TPSA) were also depicted in Figure 12. The hydrogen bond donors had been observed to be in between 0–2, hydrogen bond acceptors had fallen in range 2–5 and rotatable bonds were maximum 10. The TPSA value of all the compounds are very less with maximum TPSA for molecule **7d** which is 27.69 \AA^2 . Since this value is far less than 140 \AA^2 , the cell permeability is acceptable for all compounds and they could be completely absorbed through cell membrane.

Lipophilicity is the measure for drug affinity in lipid surroundings, which has essential use for transportation of into the cell and binding with a receptor.^[29] Hence it has important value in pharmacokinetic value. It is exerting influence on reactivity, solubility, degradation of drug, reactivity, etc. This value, partition coefficient between *n*-octanol and water ($\log P_{o/w}$), had been calculated by iLOGP,^[30] XLOGP3,^[31] WLOGP,^[32] MLOGP^[33] and SILICOS-IT^[34] methods (Figure 12). The consensus value was the arithmetic mean of all these values. These values mainly lied between 6.61 to 2.45 and the consensus had fallen

Table 2. The MM/PBSA calculation showing contribution of different energies.

Complex	Binding energy [kJ/mol]	van der Waals energy [kJ/mol]	Electrostatic energy [kJ/mol]	Polar solvation energy [kJ/mol]	SASA energy [kJ/mol]
7a	-114.337 ± 12.918	-151.103 ± 15.273	-4.267 ± 2.492	53.635 ± 10.962	-12.602 ± 0.933
7b	-128.775 ± 18.258	-164.328 ± 20.504	-3.619 ± 2.788	52.685 ± 12.243	-13.513 ± 1.157
7c	-136.940 ± 0.597	-167.259 ± 0.543	0.012 ± 0.081	45.172 ± 0.342	-14.878 ± 0.045
7d	-96.175 ± 0.399	-115.443 ± 0.389	-3.646 ± 0.070	32.833 ± 0.332	-9.922 ± 0.043

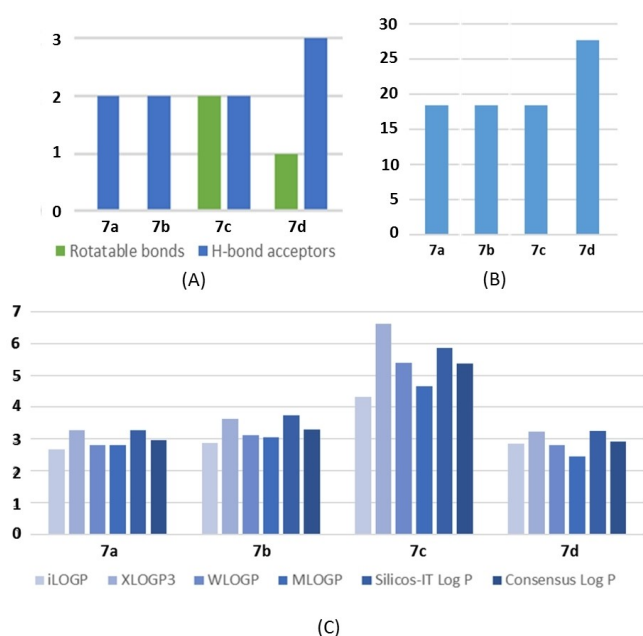


Figure 12. A) Physicochemical properties-Rotatable bonds, H-bond acceptors, and H-bond donors, B) Topological Polar Surface Area (TPSA) and C) Lipophilicity values of all compounds.

in range 5.37 to 2.92. That shows that all the molecules have good oral absorption.

The aqueous or water solubility, Log S, defines the solubility of organic compounds in water and it has impact on transport, uptake, distribution and bioavailability of compounds.^[35] It has been predicted through ESOL,^[36] AII^[37] and Silicos-IT method^[34] (Table S5). The **7c** was predicted to be poorly soluble (PS) by all three methods and others and moderately soluble (MS) or soluble (S). This suggest that the MS and S molecules could be considered for taking through oral or parenteral route.

In the pharmacokinetics study, all the compounds have high Gastro-Intestinal absorption which makes them good candidates for oral dosing. Blood brain barrier (BBB) permeability^[38] has been found to be suitable for all four compounds which implies that they have good drug distribution index. All the compounds **7a–d** were found to be Pgp substrate^[39] and hence they could be actively pumped through the cell. In the prospect of binding with metabolic enzymes CYP1 A2 inhibitor, CYP2 C19 inhibitor, CYP2 C9 inhibitor, CYP2D6 inhibitor and CYP3 A4 inhibitor binding has been stated in Table S6 and they showed degradation through at least one enzyme. Further, log K_p ,^[40] the measure for skin permeability, had been predicted and more negative values imply less permeable.

Furthermore, the drug-likeness evaluation is based on the chemical structures and physicochemical properties. This assessment had been performed using Lipinski,^[41] Ghose,^[42] Veber,^[43] Egan^[44] and Muegge^[45] methods (Table S7). The results indicated that **7a**, **7b** and **7d** follow all the rules whereas compound **7c** violates two rules. This implies that all the compounds are drug-like. Additionally, all the compounds have

sufficient bioavailability score indicating high potential for being drug candidates. The synthetic accessibility scores had also been depicted and it was found to moderate to synthesize these compounds. Moreover, all the compounds were scanned for pan-assay interference compounds (PAINS) and no compounds found positive for it. Lastly, the toxicity results concluded that all the four compounds have successfully accepted toxicities mentioned in Table S7. Thus, overall ADMET states that the molecules are not toxic and mostly they are drug-like.

Conclusion

Current study has shown the conservative nature of the 3CLpro and established this as a wonderful target for development of Covid-19 inhibitors. We introduced *cis*-fused flavonoids which are quite less explored but interesting and inexpensive compounds for the preparation of novel therapeutics. An easy and practical route for the synthesis of the *cis*-fused flavonoids i.e. 5a,10a-dihydro-11*H*-benzofuro[3,2-*b*]chromenes in good yields from easily accessible dihydroxychalcones has been developed using low-cost reagents. A new protocol i.e., NH₄OH mediated one pot tandem deprotection-cycloetherification was developed to obtain the *cis*-fused flavonoids. 3D structure of 3CLpro was further explored for docking and molecular dynamics simulation studies of newly synthesized *cis*-fused flavonoids and the binding energy and interactions are showing potential towards an excellent binding spectrum. Through docking studies the binding energy of the complexes were calculated and residual interaction were identified. Further through molecular dynamics simulation RMSD, RMSF, SASA, Hydrogen Bond, Radius of gyration of all the complexes were calculated and variation within them were observed. Clustering analysis provides us the populated clusters and the structural transition leading to the different interactive configuration obtained within the complexes to get the stable conformation. The distance calculation of the interacting and the catalytic residues (Gln 189, His 41 and Cys 149) of the protein with the atoms of the compounds were contemplated with detail study. Finally, *In-silico* ADMET study shows extremely promising results towards drug like nature of the series of fused flavonoids in terms of solubility, extremely low toxicity, etc. Thus, the current study not only provides us a series of such potential small molecules but also open a platform towards further designing of potential small molecule inhibitors against 3CLpro enzyme of SARS-CoV-2. Further *in-vitro* and *in-vivo* optimization are needed for transforming these synthesized inhibitors into established drugs.

Experimental Section

Synthetic procedures and characterization methods

Details of all synthetic procedures along with characterization methods are provided in the Supporting Information.

Structural preparation and ADMET screening for *in-silico* study

The small molecule *in-silico* structure formation was performed using ChemDraw Ultra^[46] to build in 2D. Then, the Chem3D tool was used to get three-dimensional structures of the 2D structures and mm2 based minimization,^[47] from the in-built tool of it, was carried out energy minimization. On the other hand, the 3CLpro enzyme of SARS-Cov-2 was obtained from RCSB, PDB id – 6LU7.^[48] Apo form of protease was extracted from it and then minimized using GROMACS,^[49] Linux-based open-source software. AMBER ff99sb-ILDN^[50] had been used for the minimization calculations. In order to calculate Molecular Electrostatic Potential Surfaces (MEPS), the molecular Gasteiger charges were calculated and JMOL was used to visualize the MEP surfaces.^[51]

The OpenBabel software^[52] was used to get SMILES from SDF structures of small molecules. Then absorption, distribution, metabolism and excretion (ADME) assessment had been carried out using Swiss ADME online web server.^[53] The toxicity screening was performed using the toxicophores screening from FAF-Drug 4.^[54]

Molecular docking of small molecules with target 3CL protease

After structural preparations, enzyme and ligand pdbqt file generation had been executed by AutoDock Tools 1.5.6.^[55] The grid was generated by using the template PDB 6LU7 for docking. The grid was centered at (64.039, 46.852, 58.802) and the dimension was used at 20 along all axes. The docking was performed using the AutoDock Vina.^[56] The run was performed for getting 10 states. From these resulting states, the lowest energy configuration was extracted. The interactions were calculated using the MAT web server.^[57] The visualization and figure preparation was performed by using PyMOL.^[58]

Molecular dynamics (MD) simulations

For the apo simulation, the 6LU7 proteins from 3CLpro enzyme of SARS-Cov-2 was obtained from RCSB.^[48] The simulation was performed using WebGro software (<https://simlab.uams.edu/index.php>) which is based on GROMACS.^[59] The GROMOS96 54a7 force field was chosen. The ligand topology was obtained from PRODRG 2.5 server.^[60] The apo structure and complex structures with ligands were subjected to the simulation in an explicit solvent at 300 K. Each system was subjected to the cubic box and used SPC water models for solvation. To neutralize the system, ions were added by Na⁺ and/or Cl⁻ as salt types. Energy minimizations of the proteins were performed using steepest descent in presence of solvent subjected to a max of 5000 steps. Then the equilibration process was performed after energy minimization using the NVT and NPT ensemble at 300k temperature. After equilibration, final production molecular dynamics simulations were performed for 100 ns for each system.

The analyses of the results were performed on the trajectory: the root mean square deviation (RMSD), root mean square fluctuations (RMSF) using python and the visualization, calculation were performed using PyMOL, while the clustering was performed using GROMACS^[61] and the binding affinity calculation using MM/PBSA program.^[62] PyMOL was used for figures and the plotting of the graph.

Supporting Information

The Supporting Information (SI) contains detailed descriptions of the chemical syntheses of compounds along with complete characterization data, i.e., NMR spectra, crystallographic data, docking, molecular dynamics simulations, and ADMET study data.

Acknowledgements

The authors acknowledge Prof. I. N. N. Namboothiri from the Department of Chemistry, IIT Bombay for HRMS analysis. We are also thankful to Mrs. Mamata V. Joshi and Mr. Devidas A. Jadhav of the National NMR Facility, TIFR Mumbai for recording NMR spectra for some of our samples. This work is financially supported by the Department of Atomic Energy, Government of India.

Conflict of Interest

The authors declare no conflict of interest.

Data Availability Statement

The data that support the findings of this study are available in the supplementary material of this article.

Keywords: fused flavonoids · 3CLpro inhibitors · SARS-CoV-2 · molecular docking · molecular dynamics simulation

- [1] World Health Organization. (2020). Coronavirus disease (COVID-19): weekly epidemiological update.
- [2] P. Zhou, X.-L. Yang, X.-G. Wang, B. Hu, L. Zhang, W. Zhang, H.-R. Si, Y. Zhu, B. Li, C.-L. Huang, H.-D. Chen, J. Chen, Y. Luo, H. Guo, R.-D. Jiang, M.-Q. Liu, Y. Chen, X.-R. Shen, X. Wang, X.-S. Zheng, K. Zhao, Q.-J. Chen, F. Deng, L.-L. Liu, B. Yan, F.-X. Zhan, Y.-Y. Wang, G.-F. Xiao, Z.-L. Shi, *Nature* **2020**, *579*, 270–273.
- [3] a) Y. Ohkatsu, T. Satoh, *J. Jpn. Pet. Inst.* **2008**, *51*, 298–308; b) Z. Wu, J. M. McGoogan, *Jama* **2020**, *323*, 1239.
- [4] H. Li, S.-M. Liu, X.-H. Yu, S.-L. Tang, C.-K. Tang, *Int. J. Antimicrob. Agents* **2020**, *55*, 105951.
- [5] T. Zhang, Q. Wu, Z. Zhang, *Curr. Biol.* **2020**, *30*, 1346–1351.e1342.
- [6] T. Muramatsu, C. Takemoto, Y.-T. Kim, H. Wang, W. Nishii, T. Terada, M. Shirouzu, S. Yokoyama, *Proc. Natl. Acad. Sci. USA* **2016**, *113*, 12997–13002.
- [7] L. Zhang, D. Lin, X. Sun, U. Curth, C. Drosten, L. Sauerhering, S. Becker, K. Rox, R. Hilgenfeld, *Science* **2020**, *368*, 409–412.
- [8] S. Ullrich, C. Nitsche, *Bioorg. Med. Chem. Lett.* **2020**, *30*, 127377.
- [9] A. A. Agbowuro, W. M. Huston, A. B. Gamble, J. D. A. Tyndall, *Med. Res. Rev.* **2018**, *38*, 1295–1331.
- [10] a) I. E. Orhan, F. S. Senol Deniz, *Nat. Prod. Bioprospect.* **2020**, *10*, 171–186; b) V. Mody, J. Ho, S. Wills, A. Mawri, L. Lawson, M. C. C. J. C. Ebert, G. M. Fortin, S. Rayalam, S. Taval, *Commun. Biol.* **2021**, *4*, 93; c) M. Sisay, *Pharmacol. Res.* **2020**, *156*, 104779; d) Z. Jin, X. Du, Y. Xu, Y. Deng, M. Liu, Y. Zhao, B. Zhang, X. Li, L. Zhang, C. Peng, Y. Duan, J. Yu, L. Wang, K. Yang, F. Liu, R. Jiang, X. Yang, T. You, X. Liu, X. Yang, F. Bai, H. Liu, X. Liu, L. W. Guddat, W. Xu, G. Xiao, C. Qin, Z. Shi, H. Jiang, Z. Rao, H. Yang, *Nature* **2020**, *582*, 289–293.
- [11] a) J. S. Rathee, B. S. Patro, S. Mula, S. Gamre, S. Chattopadhyay, *J. Agric. Food Chem.* **2006**, *54*, 9046–9054; b) S. Bhattacharya, S. Mula, S. Gamre, J. P. Kamat, S. K. Bandyopadhyay, S. Chattopadhyay, *Food Chem.* **2007**,

- 100, 1474–1480; c) S. Mula, D. Banerjee, B. S. Patro, S. Bhattacharya, A. Barik, S. K. Bandyopadhyay, S. Chattopadhyay, *Bioorg. Med. Chem.* **2008**, *16*, 2932–2938.
- [12] a) S. Jo, S. Kim, D. H. Shin, M.-S. Kim, *J. Enzyme Inhib. Med. Chem.* **2020**, *35*, 145–151; b) J. K. Cho, M. J. Curtis-Long, K. H. Lee, D. W. Kim, H. W. Ryu, H. J. Yuk, K. H. Park, *Bioorg. Med. Chem.* **2013**, *21*, 3051–3057.
- [13] a) T. Pillaiyar, M. Manickam, V. Namasivayam, Y. Hayashi, S.-H. Jung, *J. Med. Chem.* **2016**, *59*, 6595–6628; b) G. Li, E. De Clercq, *Nat. Rev. Drug Discovery* **2020**, *19*, 149–150.
- [14] W.-J. Liang, C.-A. Geng, X.-M. Zhang, H. Chen, C.-Y. Yang, G.-Q. Rong, Y. Zhao, H.-B. Xu, H. Wang, N.-J. Zhou, Y.-B. Ma, X.-Y. Huang, J.-J. Chen, *Org. Lett.* **2014**, *16*, 424–427.
- [15] a) M. Kuroyanagi, H. Naito, T. Noro, A. Ueno, S. Fukushima, *Chem. Pharm. Bull.* **1985**, *33*, 4792–4797; b) A. Arciniegas, A. L. Pérez-Castorena, A. Nieto-Camacho, J. L. Villaseñor, A. Romo de Vivar, *J. Mex. Chem. Soc.* **2019**, *53*; c) H. Itokawa, Z. Z. Ibraheim, Y.-F. Qiao, K. Takeya, *Chem. Pharm. Bull.* **1993**, *41*, 1869–1872.
- [16] a) L. Jiménez-González, M. Álvarez-Corral, M. Muñoz-Dorado, I. Rodríguez-García, *Phytochem. Rev.* **2008**, *7*, 125–154; b) *The Flavonoids Advances in Research Since 1986*, Routledge, **2017**; c) L. Jiménez-González, M. Álvarez-Corral, M. Muñoz-Dorado, I. Rodríguez-García, *Chem. Commun.* **2005**, 2689–2691.
- [17] N. Sepay, N. Sepay, A. Al Hoque, R. Mondal, U. C. Halder, M. Muddassir, *Struct. Chem.* **2020**, *31*, 1831–1840.
- [18] a) Y. Sawama, T. Kawajiri, S. Asai, N. Yasukawa, Y. Shishido, Y. Monguchi, H. Sajiki, *J. Org. Chem.* **2015**, *80*, 5556–5565; b) X. Wu, L. Xue, D. Li, S. Jia, J. Ao, J. Deng, H. Yan, *Angew. Chem. Int. Ed.* **2017**, *56*, 13722–13726; *Angew. Chem.* **2017**, *129*, 13910–13914; c) L. Xu, F. Liu, L.-W. Xu, Z. Gao, Y.-M. Zhao, *Org. Lett.* **2016**, *18*, 3698–3701; d) S. Rashid, B. A. Bhat, G. Mehta, *Tetrahedron Lett.* **2019**, *60*, 1122–1125.
- [19] a) Y. Jie, J. R. Niskala, A. C. Johnston-Peck, P. J. Krommenhoek, J. B. Tracy, H. Fan, W. You, *J. Mater. Chem.* **2012**, *22*, 1962–1968; b) H. Hu, J. C. Dyke, B. A. Bowman, C.-C. Ko, W. You, *Langmuir* **2016**, *32*, 9873–9882.
- [20] a) J. L. Luche, *J. Am. Chem. Soc.* **1978**, *100*, 2226–2227; b) K. Krohn, I. Ahmed, M. John, *Synthesis* **2009**, *2009*, 779–786.
- [21] H. Yuan, H. Chen, H. Jin, B. Li, R. Yue, J. Ye, Y. Shen, L. Shan, Q. Sun, W. Zhang, *Tetrahedron Lett.* **2013**, *54*, 2776–2780.
- [22] C. E. Castro, E. J. Gaughan, D. C. Owsley, *J. Org. Chem.* **1965**, *30*, 587–592.
- [23] a) S. Bhatt, K. Roy, S. K. Nayak, *Synth. Commun.* **2010**, *40*, 2736–2746; b) P. Shukla, M. Choudhary, S. Nayak, *Synlett* **2011**, *2011*, 1585–1591.
- [24] a) J. Barluenga, M. Trincado, E. Rubio, J. M. González, *J. Am. Chem. Soc.* **2004**, *126*, 3416–3417; b) Y. Lu, H. Nakatsuji, Y. Okumura, L. Yao, K. Ishihara, *J. Am. Chem. Soc.* **2018**, *140*, 6039–6043.
- [25] a) L. Panzella, M. DellaGreca, L. Longobardo, *ChemistrySelect* **2018**, *3*, 10637–10640; b) F. Mouffouk, A. Morère, S. Vidal, A. Leydet, J.-L. Montero, *Synth. Commun.* **2004**, *34*, 303–307.
- [26] a) G. Kalyan, V. Junghare, S. Bhattacharya, S. Hazra, *J. Biomol. Struct. Dyn.* **2021**, *39*, 635–649; b) M. Paul, M. Hazra, A. Barman, S. Hazra, *J. Biomol. Struct. Dyn.* **2014**, *32*, 928–949.
- [27] M. A. Hannan, R. Dash, A. A. Sohag, I. S. Moon, *Mar. Drugs* **2019**, *17*.
- [28] S. Bhattacharya, A. K. Padhi, V. Junghare, N. Das, D. Ghosh, P. Roy, K. Y. J. Zhang, S. Hazra, *Int. J. Biol. Macromol.* **2021**, *177*, 337–350.
- [29] J. A. Arnott, S. L. Planey, *Expert Opin. Drug Discovery* **2012**, *7*, 863–875.
- [30] A. Daina, O. Michielin, V. Zoete, *J. Chem. Inf. Model.* **2014**, *54*, 3284–3301.
- [31] T. Cheng, Y. Zhao, X. Li, F. Lin, Y. Xu, X. Zhang, Y. Li, R. Wang, L. Lai, *J. Chem. Inf. Model.* **2007**, *47*, 2140–2148.
- [32] S. A. Wildman, G. M. Crippen, *J. Chem. Inf. Comput. Sci.* **1999**, *39*, 868–873.
- [33] I. Moriguchi, S. Hirono, Q. Liu, I. Nakagome, Y. Matsushita, *Chem. Pharm. Bull.* **1992**, *40*, 127–130.
- [34] De Winter, H. SILICOS-IT Filter-It.
- [35] W. L. Jorgensen, E. M. Duffy, *Adv. Drug Delivery Rev.* **2002**, *54*, 355–366.
- [36] J. S. Delaney, *J. Chem. Inf. Comput. Sci.* **2004**, *44*, 1000–1005.
- [37] J. Ali, P. Camilleri, M. B. Brown, A. J. Hutt, S. B. Kirton, *J. Chem. Inf. Model.* **2012**, *52*, 420–428.
- [38] A. Daina, V. Zoete, *ChemMedChem* **2016**, *11*, 1117–1121.
- [39] F. Montanari, G. F. Ecker, *Adv. Drug Delivery Rev.* **2015**, *86*, 17–26.
- [40] R. O. Potts, R. H. Guy, *Pharm. Res.* **1992**, *09*, 663–669.
- [41] C. A. Lipinski, F. Lombardo, B. W. Dominy, P. J. Feeney, *Adv. Drug Delivery Rev.* **1997**, *23*, 3–25.
- [42] A. K. Ghose, V. N. Viswanadhan, J. J. Wendoloski, *J. Comb. Chem.* **1999**, *1*, 55–68.
- [43] D. F. Veber, S. R. Johnson, H.-Y. Cheng, B. R. Smith, K. W. Ward, K. D. Kopple, *J. Med. Chem.* **2002**, *45*, 2615–2623.
- [44] W. J. Egan, K. M. Merz, J. J. Baldwin, *J. Med. Chem.* **2000**, *43*, 3867–3877.
- [45] I. Muegge, S. L. Heald, D. Brittelli, *J. Med. Chem.* **2001**, *44*, 1841–1846.
- [46] K. R. Cousins, *J. Am. Chem. Soc.* **2011**, *133*, 8388–8388.
- [47] J.-H. Lii, S. Gallion, C. Bender, H. Wikström, N. L. Allinger, K. M. Flurchick, M. M. Teeter, *J. Comput. Chem.* **1989**, *10*, 503–513.
- [48] X. Liu, B. Zhang, Z. Jin, H. Yang, Z. Rao, *RCSB PDB Protein Data Bank*.
- [49] D. Van Der Spoel, E. Lindahl, B. Hess, G. Groenhof, A. E. Mark, H. J. C. Berendsen, *J. Comput. Chem.* **2005**, *26*, 1701–1718.
- [50] K. Lindorff-Larsen, S. Piana, K. Palmo, P. Maragakis, J. L. Klepeis, R. O. Dror, D. E. Shaw, *Proteins* **2010**, *78*, 1950–1958.
- [51] Jmol: an open-source Java viewer for chemical structures in 3D.
- [52] N. M. O’Boyle, M. Banck, C. A. James, C. Morley, T. Vandermeersch, G. R. Hutchison, *J. Cheminf.* **2011**, *3*, 33.
- [53] A. Daina, O. Michielin, V. Zoete, *Sci. Rep.* **2017**, *7*, 42717.
- [54] D. Lagorce, L. Bouslama, J. Becot, M. A. Miteva, B. O. Villoutreix, *Bioinformatics* **2017**, *33*, 3658–3660.
- [55] R. Huey, G. M. Morris, La Jolla, CA, USA: The Scripps Research Institute, Molecular Graphics Laboratory, **2008**, pp. 54–56.
- [56] O. Trott, A. J. Olson, *J. Comput. Chem.* **2010**, *31*, 455–461.
- [57] G. Kalyan, V. Junghare, S. J. S, A. Chattopadhyay, P. Mitra, S. Hazra, *Bioinformatics*, **2019**, DOI: 10.1101/605907.
- [58] W. L. DeLano, in Pymol: An open-source molecular graphics tool. CCP4 Newsletter on protein crystallography. **40**, **2002**, pp. 82–92.
- [59] *Physics computing '92: proceedings of the 4th international conference, Prague, Czechoslovakia, August 24–28, 1992*, World Scientific, Singapore, **1993**.
- [60] D. M. van Aalten, R. Bywater, J. B. Findlay, M. Hendlich, R. W. Hooft, G. Vriend, *J. Comput.-Aided Mol. Des.* **1996**, *10*, 255–262.
- [61] M. J. Abraham, T. Murtola, R. Schulz, S. Páll, J. C. Smith, B. Hess, E. Lindahl, *SoftwareX* **2015**, *1–2*, 19–25.
- [62] R. Kumari, R. Kumar, A. Lynn, *J. Chem. Inf. Model.* **2014**, *54*, 1951–1962.

Manuscript received: January 3, 2022
Accepted manuscript online: February 3, 2022
Version of record online: February 17, 2022